Longitudinal and transverse frictional drag in graphene/$LaAlO_3$/$SrTiO_3$ heterostructures

Qing Guo,[1,*] Jianan Li,[1,*] Hyungwoo Lee,[2] Jung-Woo Lee,[2] Yuhe Tang,[1] Muqing Yu,[1] Yang Hu,[1] Chang-Beom Eom,[2] Patrick Irvin,[1] and Jeremy Levy[1,†]

[1]*Department of Physics and Astronomy, University of Pittsburgh, Pittsburgh, Pennsylvania 15260, USA*

[2]*Department of Materials Science and Engineering, University of Wisconsin-Madison, Madison, Wisconsin 53706, USA*

(Received 29 November 2020; revised 16 March 2022; accepted 7 July 2022; published 20 July 2022)

Heterostructures composed of different layered materials provide novel opportunities to investigate the electronic correlations between them. Here we investigate frictional drag between graphene and $LaAlO_3/SrTiO_3$ (LAO/STO) heterostructures. The LAO/STO layer underneath the graphene is rendered conductive using conductive atomic force microscope (c-AFM) lithography, creating a two-layer system in which the LAO serves as an ultrathin (<2 nm) insulating barrier. By sourcing current in both the STO layer and graphene layer, Coulomb drag is studied in a wide range, from an STO superconducting region to a graphene quantum Hall region. Pronounced fluctuations in the frictional drag resistance are observed when the STO is superconducting. A large enhancement of drag resistance is observed when the STO becomes superconducting. Pronounced stripelike oscillations in the frictional drag appear in the quantum Hall region, both along the main channel and the transverse (Hall) configuration. The behavior is consistent with numerical simulations that model energy and momentum transfer from the STO layer to the graphene layer. These help to create a platform for graphene-based metamaterials using the programmable LAO/STO interface.

DOI: 10.1103/PhysRevB.106.045303

I. INTRODUCTION

The full nature and consequences of electronic correlations in low-dimensional electron systems remains largely open, even after many decades of intense investigation [1–9]. Electronic correlations are generally more prevalent in low-dimensional systems, and are known to give rise to phases that are not predicted by electronic band structure considerations alone. In strongly correlated electronic systems such as cuprate high-temperature superconductors [10–13], it is challenging to "peer inside" these systems or significantly tune their electronic properties other than through growth. However, relatively new two-dimensional electron systems (2DES) such as graphene and complex-oxide heterostructures offer new opportunities to investigate the effects of strong correlations between disparate material systems.

One particularly powerful approach to revealing correlated properties involves a method commonly known as "Coulomb drag," or more generally, "frictional drag," when the mechanism of interaction is non-Coulombic or unknown. When two electrical conductors are situated in close proximity, current driven through one conductor ("drive") may transfer both energy and momentum to a second conductor ("drag"), resulting in a measurable voltage (or current) [14,15]. The resulting frictional drag provides a uniquely sensitive way to measure the electronic correlations since the drag response depends on interactions without direct exchange of charge carriers. Coulomb drag has been extensively studied in GaAs quantum wells [16–22]. Other examples of correlated electron states include excitonic condensates [23–25], fractional quantum Hall phases [26,27], and Luttinger liquids [28–31].

Coulomb drag has also been studied between normal conductors and superconductors [32–38], where cross-talk is detected in superconductor-insulator-normal-metal trilayers [33]. The realization of small separation (only a few nanometers) between the bilayer of two-dimensional electron gases (2DEGs) in bilayer-graphene systems lead to many novel phenomena, including interlayer energy transfer drag [39], giant magnetodrag effect [40], and magnetic-field induced superfluid state [41,42]. Recently, unconventional superconductivity has been observed in a two-dimensional superlattice made from "magic angle" twisted bilayer graphene [43,44]. In this system, coupling between the two graphene layers, combined with a superlattice potential from the Moiré interference, leads to new emergent phases.

The $LaAlO_3/SrTiO_3$ (LAO/STO) interface offers an ideal platform [45] for combining the rich physics of graphene with that of a tunable 2D superconductor. The LAO/STO system exhibits a rich variety of electronically tunable properties such as superconductivity [46,47], magnetism [48], and spin-orbit coupling [49]. The LAO/STO interface also exhibits a hysteretic metal-insulator transition [5,50], which can be controlled locally using conductive atomic force microscopy (c-AFM) lithography and used to create a range of mesoscopic devices [51,52]. The LAO/STO interface properties are dominated by the electrons from STO, while the LAO provides a wide-band-gap insulating layer.

The G/LAO/STO (G stands for graphene) hybrid system allows the study of Coulomb drag between superconducting STO and nonsuperconducting graphene, separated by a

*These authors contributed equally to this work.
†jlevy@pitt.edu

thin (<2 nm) LAO layer. Frictional drag has been investigated in LAO/STO heterostructures [5], where it is possible to create quasi-one-dimensional conducting channels in the STO layer through the technique of conductive atomic force microscope (c-AFM) lithography [51]. In this technique, LAO/STO structures with LAO thickness near the metal-insulator transition [50] are positively charged with protons coming from adsorbed water [53], and the STO layer just beneath becomes conductive at room temperature and superconducting [47] at lower temperatures ($T < T_C \approx 300$ mK). Tang *et al.* have shown that strong frictional drag effects exist between LAO/STO nanowires, and that the interactions are non-Coulombic in nature [15] and significantly enhanced in the superconducting state [54].

Heterostructures formed between graphene and LAO/STO heterostructures provide novel opportunities to investigate interactions within and between these two rich systems [55,56]. To create the frictional drag geometry, rectangular areas of LAO/STO are rendered conductive underneath the graphene using c-AFM lithography. In this case, the LAO layer serves as an ultrathin insulating barrier. Frictional drag measurements are performed between the two conducting layers; when the LAO/STO is the drive layer, frictional drag for both the longitudinal and transverse (Hall) configuration are measured. Experiments where graphene is the drive layer and LAO/STO is the drag layer are performed under conditions where the LAO/STO system is in the superconducting and nonsuperconducting states.

II. DEVICE FABRICATION AND CHARACTERIZATION

G/LAO/STO devices consist of a graphene layer and two-dimensional electron layer (2DEL) in the STO, near the LAO/STO interface. The graphene and STO layers are separated by 8 unit cells (2.8 nm) of insulating LAO, grown on STO by pulsed laser deposition (PLD). The graphene is grown by chemical vapor deposition (CVD) on oxygen-free electronic-grade copper flattened with a diamond turning machine [57]. Graphene is transferred onto the LAO surface with the wet-transfer technique by using perfluoropolymer Hyflon AD60 as a transferring layer. Graphene is patterned into Hall bars by standard photolithography. The photoresist (AZ4210) is spin coated onto the graphene film (4000 rpm for 30 s, heating at 95°C for 2 min). Reactive ion etching (RIE) with O_2 plasma is used to etch the exposed area of the graphene sheet except for the graphene bar. Particles and contaminants on graphene from wet transfer and photolithography are brushed away using a contact-mode AFM scan sequence. Experiments with G/LAO/STO have been underway since 2013, with the first paper published in 2015 [58]. The mobility of graphene exfoliated on LAO surfaces is nowhere near the record-high values obtained for hBN-encapsulated graphene. However, they do appear to be higher, on average, than devices fabricated directly on SiO_2. A 2DEL is formed during c-AFM writing. Graphene is scanned with a doped silicon AFM tip in contact mode with a contact force of 15–20 nN and scanning speed between 2 and 20 μm/s. A bias voltage $V_{\text{tip}} = 20$ V is used to create a conductive LAO/STO interface underneath the graphene [59]. To prevent any leakage current from conductive AFM tip to graphene, a 1 GΩ resistor is connected to

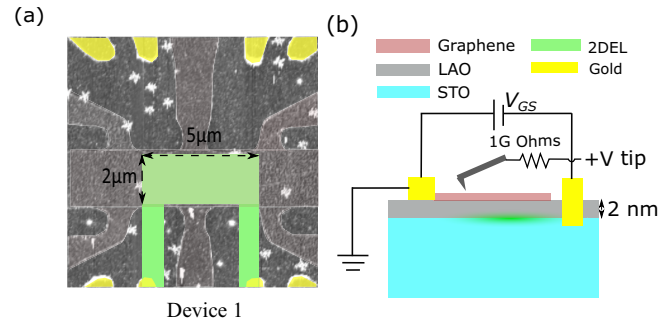

FIG. 1. (a) AFM image of the G/LAO/STO device 1. Graphene is patterned into a Hall bar structure on top of the LAO surface. The green shaded areas represent regions where the STO is locally patterned by c-AFM lithography into a conductive state. A 2×5 μm^2 conducting region is patterned under the graphene channel, and connected by 1-μm-wide channels to Ti/Au electrodes that are etched through the interface. (b) Side-view schematic of the c-AFM lithography process.

the tip. The impact of c-AFM lithography itself on graphene quality was not quantitatively characterized here but has been considered early on in our previous study [56]. No discernible difference in the Raman spectra (e.g., appearance of D peak) between as-deposited and c-AFM written graphene was observed.

The device geometry is illustrated in Fig. 1(a). Figure 1(b) illustrate the c-AFM lithography technique used to create conductive areas in the STO. The conducting pattern sketched underneath the graphene is rectangular in shape with a width of 2 μm and length of 5 μm. This conducting region extends outside the graphene and connects to one of the edge electrodes [Fig. 1(a)]. The carrier density n of graphene and STO can be varied by the gate voltage V_{GS} between them. In order to estimate the change of carrier density in graphene, we employ a capacitive model in which the capacitance between the graphene and LAO layer is estimated to be $C = 4.5$ μF/cm^2. With this model, the change of carrier density in graphene can be calculated as $\Delta n = CV_{\text{GS}}/e$. The graphene can subsequently gate the STO layer via a field effect [59].

The impact of backgate V_{bg} on the doping level of graphene is shown in Fig. 2. Due to the shielding effect of LAO/STO, the carriers in graphene cannot be tuned effectively in the electron side. In the p-type doped region, the Landau levels are visible. The density of the graphene layer can be tuned

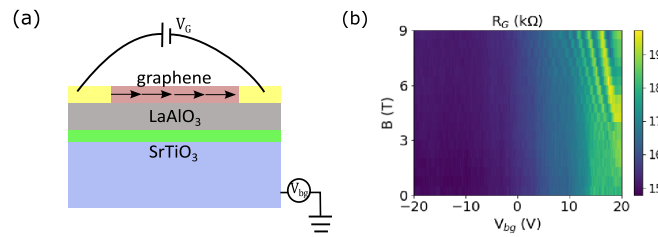

FIG. 2. Graphene resistance as a function of magnetic field and carrier density. (a) Schematic diagram for measuring the graphene resistance. (b) Landau levels are visible. Graphene is n-type doped.

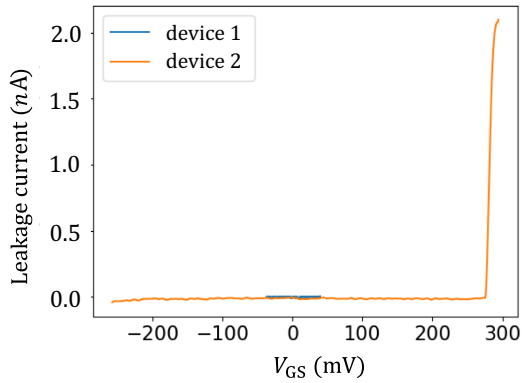

FIG. 3. Leakage test across graphene and STO.

with the interlayer gate voltage (V_{GS}) utilizing LAO as the dielectric layer.

Figure 3 is the typical leakage test for devices 1 and 2. V_{GS} is applied between graphene and STO, the leakage current is measured between graphene and STO. In order to ensure the drag resistances are not influenced by electron tunneling between the two nanowires, all measurements are performed well below the measured interwire breakdown voltage of each device.

Coulomb drag measurements are performed by sourcing current in one layer and measuring a voltage in the other layer. In an idealized experiment, a constant (DC) current I_1 is passed through the active layer. The passive layer is kept isolated at the same time. The voltage V_2 induced in the passive layer is proportional to I_1. The coefficient drag resistance $R_D = -V_2/I_2$ is a direct measure of interlayer interactions [14]. During this process, the violation of Onsager relation might happen, e.g., $R_{SG} \neq R_{GS}$. The drag layer sets the scale for R_{SG} or R_{GS} [60]. We first describe experiments in which we source current I_G in the graphene (G) and measure a voltage V_S in the STO (S). The source current I_G consists of a DC component I_G^0 and an AC component I_G^ω at angular frequency ω: $I_G = I_G^0 + I_G^\omega \cos(\omega t)$. Sourcing current in this way generally yields a combined DC and AC voltage in the STO: $V_S = V_S^0 + V_S^\omega \cos(\omega t)$. The (differential) drag resistance in STO may then be calculated as $R_{SG} \equiv V_{SG}^\omega / I_S^\omega$, where V_S^ω and I_S^ω are separately measured using lock-in amplification. Here we explore the dependence of R_{SG} on a variety of parameters including I_G^0, V_{GS}, and plane-perpendicular magnetic field B. Except where noted otherwise, all measurements are performed at $T < 100$ mK. We similarly perform experiments in which current is sourced in the STO layer $I_S = I_S^0 + I_S^\omega \cos(\omega t)$, yielding voltages in the graphene $V_S = V_S^0 + V_S^\omega \cos(\omega t)$, and define $R_{GS} \equiv V_{GS}^\omega / I_G^\omega$, which corresponds to the (differential) drag resistance in graphene due to currents sourced in the STO layer. Meanwhile, $R_G \equiv V_G^\omega / I_G^\omega$ corresponds to two-terminal resistance in graphene and $R_S \equiv V_S^\omega / I_S^\omega$ corresponds to two-terminal resistance in STO. Both graphene and STO are connected to metallic electrodes and share a common ground. In order to ensure that the drag resistances are not influenced by electron tunneling between layers, leakage tests are performed before all measurements.

III. DRAG IN STO

The drag resistance R_{GS} in Fig. 4(e) exhibits the main feature: A stripelike modulation as the carrier density Δn is changing. The stripelike feature is also manifested in graphene resistance as a function of B and Δn [Fig. 4(c)] and can be attributed to universal conductance fluctuations (UCFs) [61]. At low temperatures, the quantum transport of electrons becomes coherent and leads to quantum interference. The UCFs take place when a coherent electron wave scatters while traversing a disordered conductor. As the same electrons are responsible for Coulomb drag, it is natural to expect that the drag resistivity also exhibits mesoscopic fluctuations [14,62]. The drag fluctuations change sign randomly but reproducibly between positive and negative values. Though the drag conductance is alternating between positive and negative, the sign of carriers is not changing. The strong sign-changing drag can be explained by interaction-induced spatial correlations due to the electron-hole symmetry breaking. We explain the sign change by the sensitivity of mesoscopic drag in the ballistic regime, to local properties of the system. Contrary to UCFs, fluctuations of the drag are larger than the average, so that drag resistivity randomly changes its sign [62], which has also been observed by [39,62]. The large drag resistance in STO is correlated with the superconducting state in the STO, decaying when the upper critical magnetic field is reached. The asymmetry of graphene resistance R_G [Fig. 4(c)] in magnetic field is ascribed to a known magnetocaloric effect when the magnetic field changes direction in the dilution refrigerator [63]. The drag resistance R_{SG} in Fig. 4(b) exhibits a large drag resistance near zero magnetic field, probably related to the superconductivity of STO, which is presented by the dark line at 0 T in Fig. 4(f). Typically $\mu_0 H_C \sim 0.3$ T [64]; however, in this instance the critical field is strongly suppressed, around 50 Oe. The assignment of this feature to superconductivity is based on extensive knowledge of STO-based devices. The superconducting state is fragile, and T_c is generally low (below 300 mK). The superconducting phase does not seem to affect the frictional drag in graphene, unlike the case for frictional drag between two LAO/STO nanowires [54]. Drag resistance R_{SG} is also studied in graphene while current is running in STO. Drive current $I_S = I_S^\omega \cos \omega t$ with $\omega/2\pi = 9.468$ Hz and $I_G^\omega = 18$ nA is applied in STO. However, the drag in graphene is not enhanced when the STO is superconducting.

The drag resistance R_{SG} in STO is studied as a function of DC current in graphene. As shown in Fig. 5, a drive current $I_G = I_G^0 + I_G^\omega \cos \omega t$ ($I_G^\omega = 28$ nA) is passed through the graphene while I_G^0 is varied from -650 to 650 nA. The corresponding V_G is -20 to 20 mV for Fig. 5(d) and -15 to 15 mV for Fig. 5(f). I_G^0 is calculated as an integration of I_G^ω under V_G as $I_G^0 = \int dI_G^\omega$. The current in our sample (28 nA) is within a commonly used range compared with other graphene transport experiments [65] with similar size and resistance. The heating effect can be ignored since the driving current is relatively small compare with those current-induced heating graphene devices. According to [66], heating up a comparable graphene size with 100 mK will need 10^3 to 10^4 higher current density.

For both devices shown here and other devices, the drag resistance as a function of driving current are asymmetric away

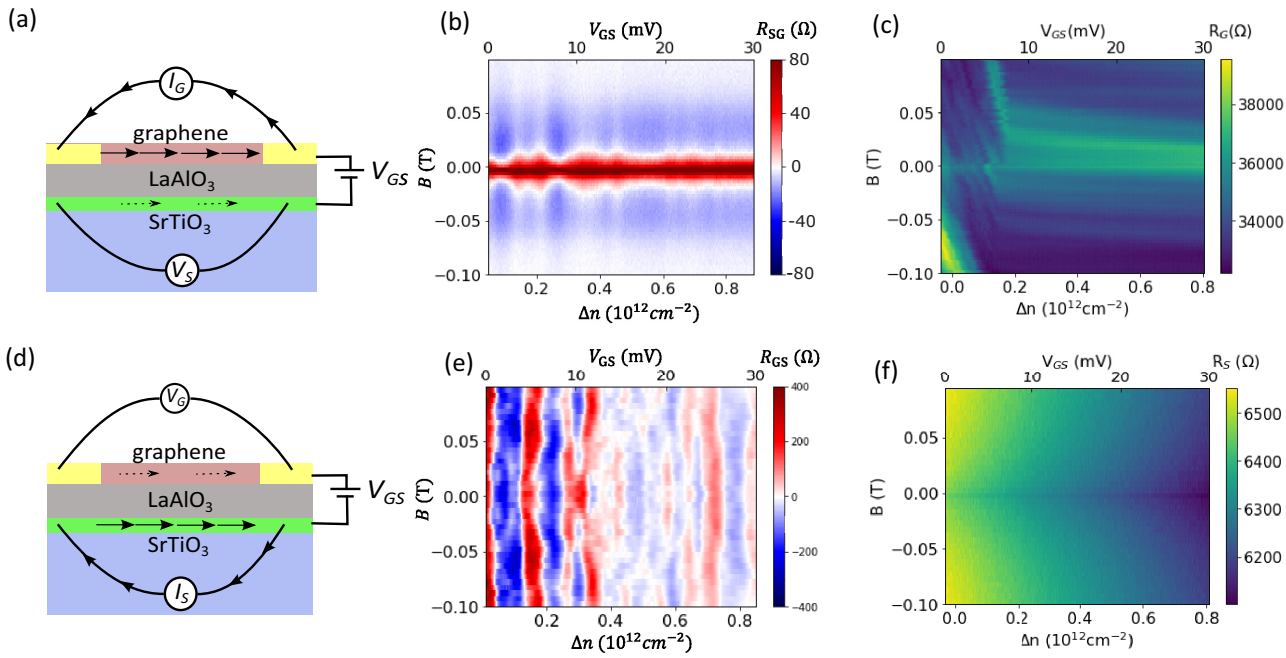

FIG. 4. Drag resistance measured in device 1. (a) Schematic diagram for measuring the drag signal in STO. A drive current is passed through the graphene. A bias voltage V_{GS} is maintained between graphene and STO. Graphene carrier density will change as R_{GS} varies. (b) The drag resistance in STO measured at $T = 50$ mK versus magnetic field. The drag resistance is enhanced in a low magnetic field. (c) Two-terminal resistance of graphene. (d) Schematic diagram for measuring drag resistance in graphene. Drive current $I_S = I_S^{\omega} \cos \omega t$ with $I_S^{\omega} \approx 18$ nA. (e) Drag resistance in graphene with drive current running through STO. (f) Two-terminal resistance of STO.

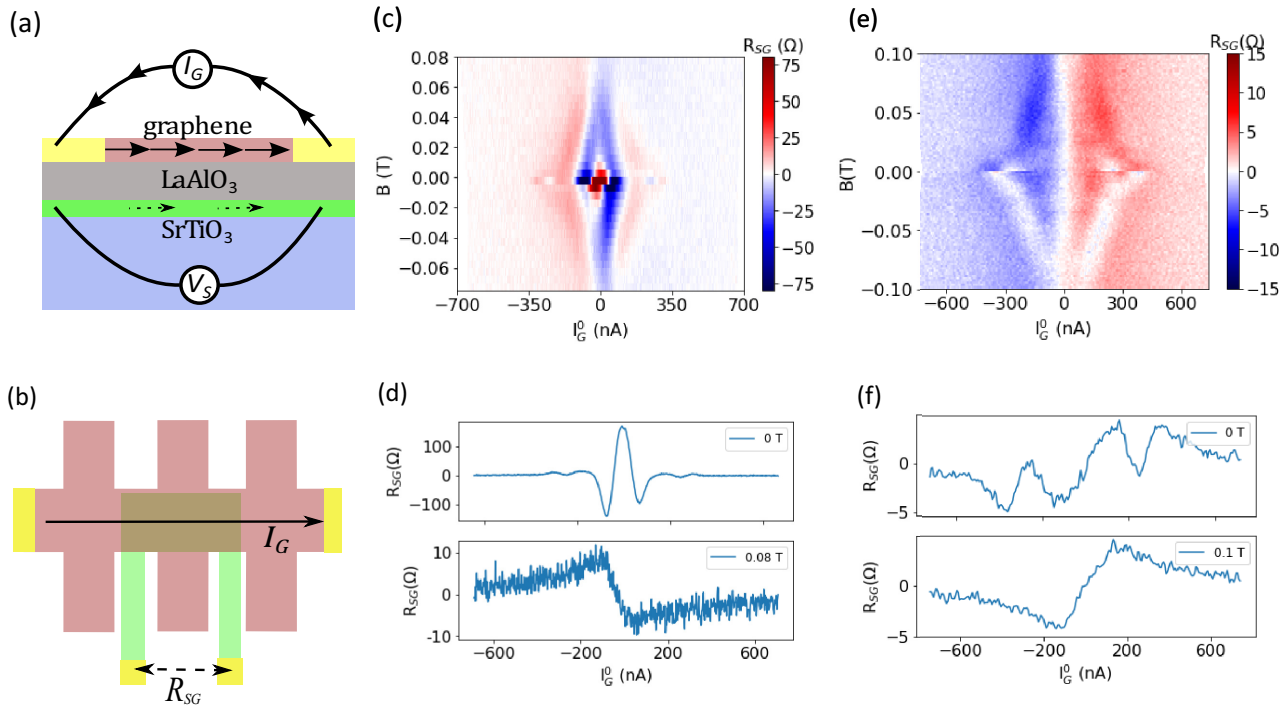

FIG. 5. (a) Schematic diagram for measuring drag resistance in STO (side view). (b) Schematic diagram for measuring drag resistance in STO (top view). (c) Drag resistance R_{GS} in STO (device 1) as a function of drive current and magnetic field. (d) R_{GS} vs drive current at $B = 0$ T and $B = 0.08$ T. Drag resistance is greatly enhanced at zero magnetic field. (e) Drag resistance R_{GS} in STO (device 3) as a function of drive current and magnetic field. (f) R_{GS} vs drive current at $B = 0$ T and $B = 0.1$ T.

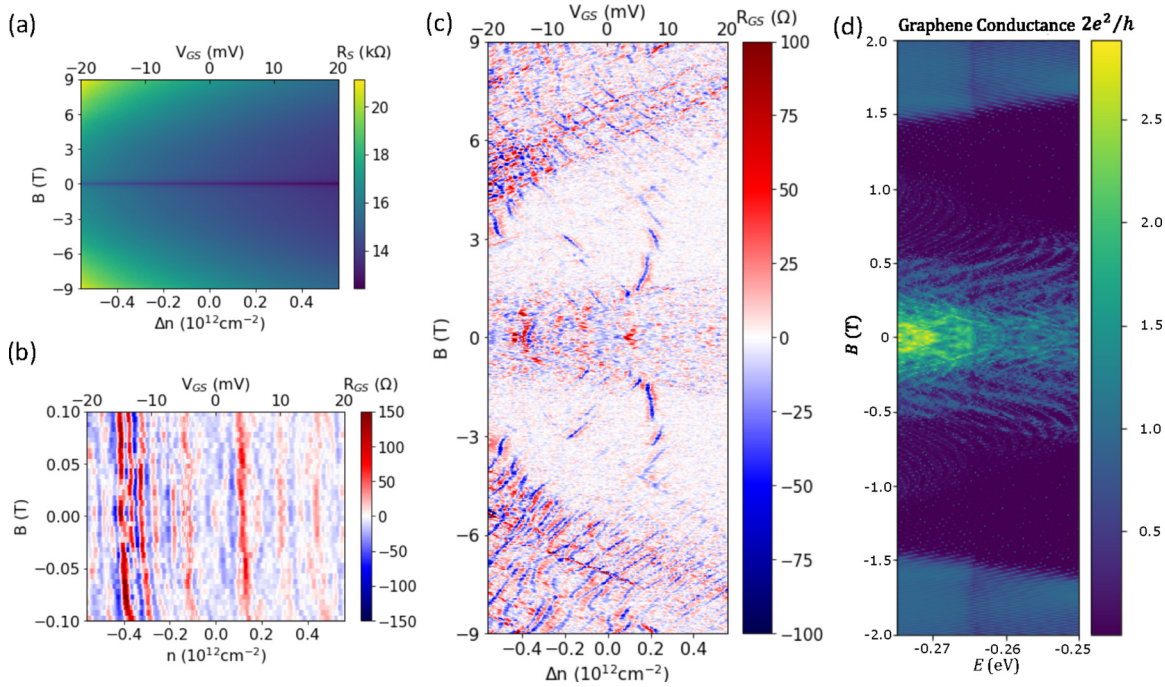

FIG. 6. Drag resistance in device 2 graphene in a larger magnetic field range. (a) STO resistance R_S. (b) Drag resistance R_{GS} is measured in graphene from $B = -0.1$ to 0.1 T, which is quite consistent with device 1. (c) Drag resistance R_{GS} is measured in graphene from $B = -9$ to 9 T. (d) Conductance of graphene is calculated by a tight-binding quantum transport calculation (Kwant) based on the designed geometry of the measured device.

from the superconducting region, as shown in the bottom subpanel of Figs, 5(d) and 5(f). In the center of the superconducting region, the drag is a superimpose of symmetric and asymmetric signal, as with respect to driving current, shown in the top subpanel of Figs. 5(d) and 5(f). As the magnetic field increases, the drag signal becomes asymmetric. This phenomenon is similar to the result of the frictional drag between superconducting LAO/STO nanowires [15], which exhibits a strong and highly symmetric component in the superconducting region, and distinct from the antisymmetric drag resistance between LAO/STO nanowires in the normal state.

The drag resistance shows nonlinearity with driving current in Figs. 5(d) and 5(f). Nonequilibrium frictional drag in graphene/LAO/STO shares some characteristics with coupled LAO/STO nanowires. Frictional drag in that system is characterized by long-range non-Coulombic interactions whose origins appear to be related to naturally forming ferroelastic domain patterns. It is unclear if the physical mechanisms are similar with the graphene/STO structures reported here, although the two systems do share similar dependencies of the frictional drag on the magnitude of the current bias. A similar temperature dependence with Fig. 9 is also found for this system, at least over the temperature range that was investigated.

IV. DRAG IN GRAPHENE

Drag resistance in graphene is investigated in a lager magnetic field range for device 2 in Fig. 6. Drive current $I_S = I_S^\omega \cos\omega$ with $\omega/2\pi = 9.468$ Hz and $I_S^\omega = 5$ nA is passed through STO. At small magnetic fields [Fig. 6(b)], the drag resistance in device 2 also shows giant fluctuations, quite consistent with device 1 [Fig. 4(e)]. We observe magnetodrag resistance oscillations that are tuned by carrier density and magnetic field. The drag signal is strong at both low and high magnetic fields. In the intermediate magnetic field regime,

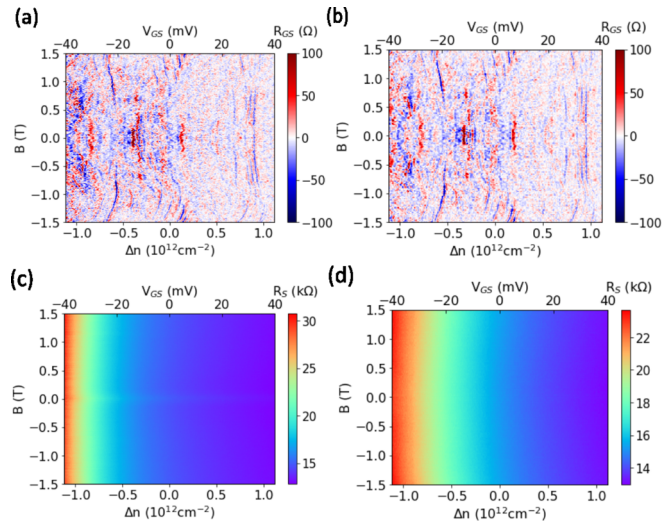

FIG. 7. (a) Drag resistance is measured in graphene at $T = 50$ mK from $B = -1.5$ to 1.5 T when LAO/STO is in superconducting state shown in (c). (b) Drag resistance is measured in graphene at 50 mK from -1.5 to 1.5 T when LAO/STO is no longer in a superconducting state shown in (d). (c) AC current measured in graphene when $I_S^0 = 140$ nA is applied to one of the STO leads. (d) AC current measured in graphene when a small $I_G^0 = 350$ nA is applied.

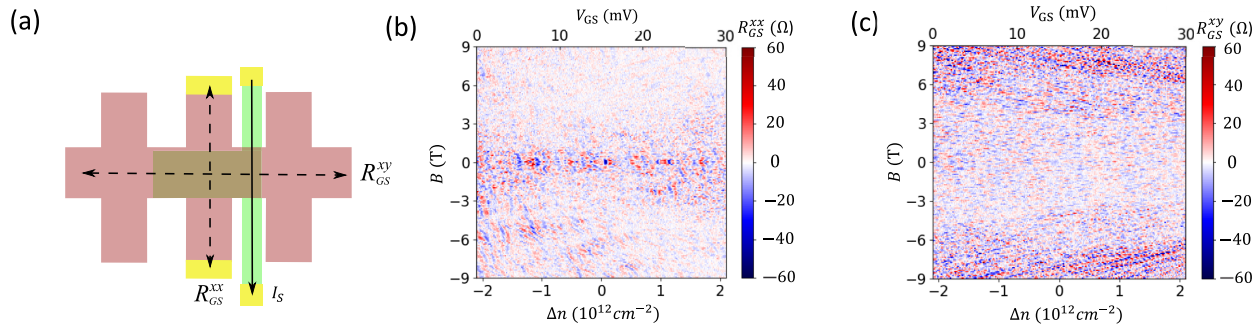

FIG. 8. Graphene drag resistance R_{GS} in longitudinal direction and transverse direction from device 3 at $T = 2$ K. (a) Configuration for longitudinal drag and transverse drag measurements. (b) Graphene drag resistance measured in the longitudinal direction. (c) Graphene drag resistance measured in the transverse direction.

the drag signal decreases to zero. In the high magnetic field region (3 to 5 T), the magnitude of the drag fluctuations as a function of Δn is roughly the same as that as a function of B. The drag resistance is dominated by the properties of the drag layer. The purpose of the drive layer is to impart energy and momentum; after that, the physics is dominated by the electronic properties of the drag layer. To better understand drag in graphene, We calculate the conductance of graphene using the Kwant package [67] [shown in Fig. 6(d)]. The numerical simulation results show higher conductance of graphene at low and high magnetic fields, consistent with the measurement of drag resistance shown in Fig. 6(c). The conductance drop between 0.5 to 1.5 T in Fig. 6(d) is due to localization of the wave function at $B = 1$ T [Fig. 10(c)]. Given the fact that drag resistance is usually proportional to drive current, we conclude that the magnetodrag resistance in STO is essentially following the tendency of conductance in graphene.

The STO resistance R_S is shown in Fig. 6(a). The dark blue region at zero magnetic field indicates the superconductivity of STO. Unlike the drag resistance in STO, the drag resistance in graphene is not enhanced when the STO is superconducting. To our knowledge, the drag signal in graphene at small magnetic fields is not correlated with the superconductivity in STO. The drag features in graphene remain almost the same when we increase the DC component of the drive current to destroy the superconductivity in STO.

In Fig. 7, drag resistance in graphene is shown when drive current is in superconducting and nonsuperconducting region. Drive current $I_S = I_S^0 + I_S^\omega \cos \omega t$ with $\omega/2\pi = 9.468$ Hz and $I_S^\omega = 16$ nA is running through STO. Here we can change the DC component of sourcing current in STO. In Fig. 7(c) the drive current I_S^0 is 140 nA. The superconductivity still exists, but weaker. In Fig. 7(d) the I_S^0 increases to 350 nA, completely destroying the conductivity in STO. The drag resistances in Figs. 7(a) and 7(b) are almost the same, which demonstrates the drag feature is not determined by the superconductivity in STO. The drag resistance versus B shows reproducible mesoscopic fluctuations.

V. LONGITUDINAL AND TRANSVERSE DRAG

We investigate the longitudinal and transverse drag resistance in graphene using a LAO/STO pattern as shown in Fig. 8. Drive current $I_S = I_S^\omega \cos \omega t$ with $\omega/2\pi = 9.468$ Hz and $I_S^\omega = 16$ nA is applied to the STO. The longitudinal drag resistance exhibits oscillations from -2 to 2 T. In the high magnetic field region, the longitudinal drag resistance is almost zero. However, the transverse drag resistance shows oscillations in the high magnetic field region. In a small magnetic field, electrons in the drive layer have a larger cyclotron radius such that momentum along the current direction will be transferred to the drag layer. On the other hand, in a high magnetic field, electrons in the drag layer have a smaller cyclotron radius and thus can move perpendicular to current direction. Momentum perpendicular to current direction is then transferred to electrons in the drag layer. In such a way, drag resistance is more prominent in the Hall direction under high field.

VI. CONCLUSION

In this paper we have shown the essential features of Coulomb drag in several G/LAO/STO devices. Both R_{GS} and R_{SG} can be tuned as a function of carrier density and magnetic field. Numerical simulation shows the localization of edge states in graphene in a magnetic field, which corresponds to the dismiss of drag signal in STO in the intermediate magnetic field range. Drag resistance in STO, R_{SG}, is greatly enhanced when the STO is superconducting. Moreover, the magnetodrag resistance in graphene has different behavior in the longitudinal and Hall directions. The longitudinal drag resistance shows more features from -2 to 2 T, while the Hall drag resistance has more prominent features in a high magnetic field. Hybrid G/LAO/STO offers a novel platform for creating programmable graphene-based devices, in which the LAO/STO layer introduces a spatially modulated gate-tunable potential, and also couples weakly to the graphene layer via frictional drag.

Note added. During the writing of this manuscript we became aware of related research by Tao *et al.* [68].

ACKNOWLEDGMENTS

This research was supported by the Office of Naval Research (N00014-16-1-3152), National Science Foundation and US-Israel Binational Science Foundation (DMR-1609519 and PHY-1913034), and Vannevar Bush Faculty Fellowship

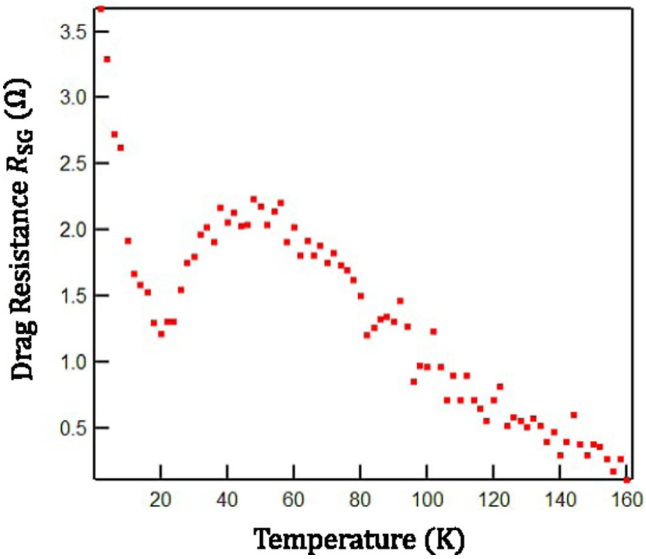

FIG. 9. Drag resistance in STO as a function of temperature.

program sponsored by the Basic Research Office of the ASD(R&E) (ONR N00014-15-1-2847), and Office of Naval Research (N00014-20-1-2481). The work at University of Wisconsin-Madison is funded by the Gordon and Betty Moore Foundation's EPiQS Initiative, Grant GBMF9065 to Chang-Beom Eom and the Air Force Office of Scientific Research (FA9550-15-1-0334).

APPENDIX A: TEMPERATURE DEPENDENCE OF DRAG RESISTANCE

The temperature dependence of drag resistance in STO is shown in Fig. 9. The drag resistance diverges below 20 K. From 20 to 50 K, the drag resistance increase with temperature. Beyond 50 K, the drag resistance starts dropping down to zero. This temperature dependence is inconsistent with either Coulombic interaction or other non-Coulombic interactions, such as virtual phonon exchange [18,69,70].

APPENDIX B: KWANT SIMULATION

The numerical calculations of graphene conductivity were performed using the Kwant code [67]. All dimensionalities and geometries are described by a tight-binding model. Transport properties are obtained from the scattering matrix include conductance, scattering matrix, wave functions, and many other quantities. The graphene device has the dimensions $L \times H$. L is $100a$ and H is $20a$, where $a \approx 0.142$ nm is the length of the carbon-carbon bond. Two graphene leads are attached to graphene to obtain the conductance of graphene. A potential well is added to graphene in the center. The height of the well is 0.3 eV.

Numerical simulation of graphene conductance calculated by Kwant is shown in Fig. 10. Kwant is a Python package for numerical calculations based on tight-binding models. The scattering matrix and the wave function inside the scattering region are solved by the recursive Green's function algorithm (RGF). Real physical quantities such as energy and magnetic field can be passed to the system by an initial dictionary. The

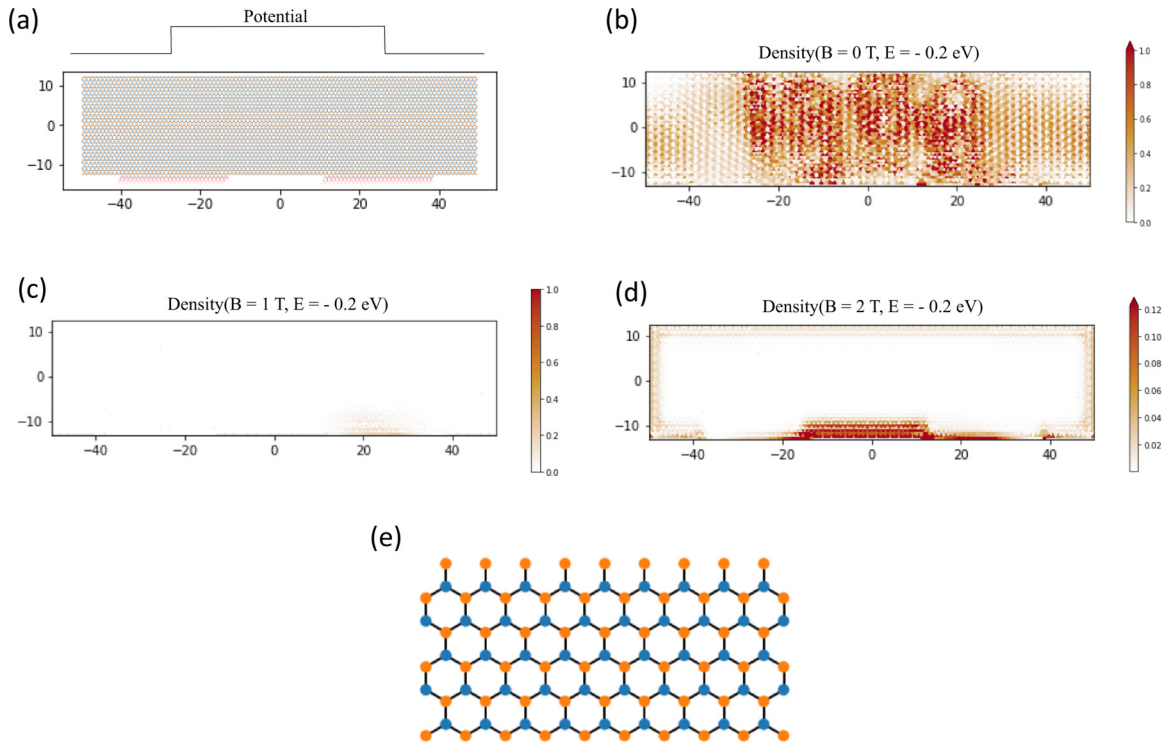

FIG. 10. Kwant simulation of graphene. (a) Graphene device with two leads attached. (b), (c), and (d) Wave function density plot under $B = 0$, 1, and 2 T. (e) Graphene lattice. Yellow and blue dots denote the two sublattices of graphene. Black lines between two atoms are the hopping terms.

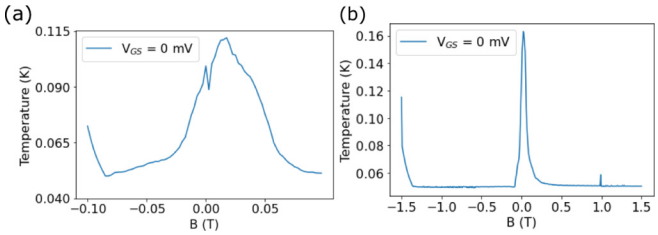

FIG. 11. Magnetocaloric effect in STO. (a) The temperature map during the measurement of Fig. 4(c). (b) The temperature map during the measurement of Fig. 7(d).

function kwant.Smatrix calculates the scattering matrix of the system at a given energy and magnetic field. The function kwant.ldos returns the local density of states in the scattering region. Our device is depicted in Fig. 10(a). The honeycomb lattice has two basis atoms [Fig. 10(e)]. A potential well is added to graphene in the center as shown in Fig. 10(a). The height of the well is 0.3 eV.

Wave function density is shown in Figs. 10(b) to 10(d), with the magnetic field varied from 0 to 2 T. At zero magnetic field, wave function is distributed in the whole device while it vanishes at 1 T. As the magnetic field increases to 2 T, the wave function is more localized at the edge of the device. These density plots in graphene also give us a insight about how edge states evolve under a magnetic field can affect the drag signal in STO. Typically, drag signal is proportional to driving current. This can explain why the drag signal is stronger in high and low magnetic fields than intermediate magnetic field.

APPENDIX C: MAGNETOCALORIC EFFECT

The asymmetry in magnetic field can be ascribed to a known magnetocaloric effect in the dilution refrigerator when the magnetic field changes direction. It also appears in other figures, such as Figs. 5(d) and 5(f), the drag resistance is not strictly symmetric for current. To better illustrate the magnetocaloric effect, here we include the temperature monitor in Figs. 11(a) and 11(b) for Figs. 4(c) and 7(d). In Fig. 11(a) the temperature drifting is due to the magnetocaloric effect.

[1] W. Sommer, Liquid Helium as a Barrier to Electrons, Phys. Rev. Lett. **12**, 271 (1964).

[2] K. S. Novoselov, A. K. Geim, S. V. Morozov, D. Jiang, M. I. Katsnelson, I. V. Grigorieva, S. V. Dubonos, and A. A. Firsov, Two-dimensional gas of massless dirac fermions in graphene, Nature (London) **438**, 197 (2005).

[3] Y. Kozuka, A. Tsukazaki, D. Maryenko, J. Falson, S. Akasaka, K. Nakahara, S. Nakamura, S. Awaji, K. Ueno, and M. Kawasaki, Insulating phase of a two-dimensional electron gas in $Mg_xZn_{1-x}O$/ZnO heterostructures below $\nu = 1/3$, Phys. Rev. B **84**, 033304 (2011).

[4] H. Y. Hwang, Y. Iwasa, M. Kawasaki, B. Keimer, N. Nagaosa, and Y. Tokura, Emergent phenomena at oxide interfaces, Nat. Mater. **11**, 103 (2012).

[5] A. Ohtomo and H. Hwang, A high-mobility electron gas at the $LaAlO_3/SrTiO_3$ heterointerface, Nature (London) **427**, 423 (2004).

[6] A. Kumar, G. A. Csáthy, M. J. Manfra, L. N. Pfeiffer, and K. W. West, Nonconventional Odd-Denominator Fractional Quantum Hall States in the Second Landau Level, Phys. Rev. Lett. **105**, 246808 (2010).

[7] W. Pan, N. Masuhara, N. S. Sullivan, K. W. Baldwin, K. W. West, L. N. Pfeiffer, and D. C. Tsui, Impact of Disorder on the 5/2 Fractional Quantum Hall State, Phys. Rev. Lett. **106**, 206806 (2011).

[8] K. V. Klitzing, G. Dorda, and M. Pepper, New Method for High-Accuracy Determination of the Fine-Structure Constant Based on Quantized Hall Resistance, Phys. Rev. Lett. **45**, 494 (1980).

[9] M. C. Geisler, J. H. Smet, V. Umansky, K. von Klitzing, B. Naundorf, R. Ketzmerick, and H. Schweizer, Detection of a Landau Band-Coupling-Induced Rearrangement of the Hofstadter Butterfly, Phys. Rev. Lett. **92**, 256801 (2004).

[10] K. Lang, V. Madhavan, J. Hoffman, E. W. Hudson, H. Eisaki, S. Uchida, and J. Davis, Imaging the granular structure of high-T_c superconductivity in underdoped $Bi_2Sr_2CaCu_2O_{8+\delta}$, Nature (London) **415**, 412 (2002).

[11] J. Lee, K. Fujita, K. McElroy, J. Slezak, M. Wang, Y. Aiura, H. Bando, M. Ishikado, T. Masui, J.-X. Zhu *et al.*, Interplay of electron–lattice interactions and superconductivity in $Bi_2Sr_2CaCu_2O_{8+\delta}$, Nature (London) **442**, 546 (2006).

[12] Y. Kohsaka, C. Taylor, K. Fujita, A. Schmidt, C. Lupien, T. Hanaguri, M. Azuma, M. Takano, H. Eisaki, H. Takagi *et al.*, An intrinsic bond-centered electronic glass with unidirectional domains in underdoped cuprates, Science **315**, 1380 (2007).

[13] P. E. Allain and J.-N. Fuchs, Klein tunneling in graphene: Optics with massless electrons, Eur. Phys. J. B **83**, 301 (2011).

[14] B. N. Narozhny and A. Levchenko, Coulomb drag, Rev. Mod. Phys. **88**, 025003 (2016).

[15] Y. Tang, A. Tylan-Tyler, H. Lee, J.-W. Lee, M. Tomczyk, M. Huang, C.-B. Eom, P. Irvin, and J. Levy, Long-range non-Coulombic electron–electron interactions between $LaAlO_3/SrTiO_3$ nanowires, Adv. Mater. Interfaces **6**, 1900301 (2019).

[16] T. J. Gramila, J. P. Eisenstein, A. H. MacDonald, L. N. Pfeiffer, and K. W. West, Mutual Friction Between Parallel Two-Dimensional Electron Systems, Phys. Rev. Lett. **66**, 1216 (1991).

[17] J. Eisenstein, New transport phenomena in coupled quantum wells, Superlattices Microstruct. **12**, 107 (1992).

[18] T. J. Gramila, J. P. Eisenstein, A. H. MacDonald, L. N. Pfeiffer, and K. W. West, Evidence for virtual-phonon exchange in semiconductor heterostructures, Phys. Rev. B **47**, 12957 (1993).

[19] T. J. Gramila, J. P. Eisenstein, A. MacDonald, L. N. Pfeiffer, and K. W. West, Measuring electron-electron scattering rates through mutual friction, Phys. B: Condens. Matter **197**, 442 (1994).

[20] U. Sivan, P. M. Solomon, and H. Shtrikman, Coupled Electron-Hole Transport, Phys. Rev. Lett. **68**, 1196 (1992).

[21] P. M. Solomon and B. Laikhtman, Mutual drag of 2D and 3D electron gases in heterostructures, Superlattices Microstruct. **10**, 89 (1991).

[22] P. M. Solomon, P. J. Price, D. J. Frank, and D. C. La Tulipe, New Phenomena in Coupled Transport between 2D and 3D Electron-Gas Layers, Phys. Rev. Lett. **63**, 2508 (1989).

[23] M. Kellogg, I. B. Spielman, J. P. Eisenstein, L. N. Pfeiffer, and K. W. West, Observation of Quantized Hall Drag in a Strongly Correlated Bilayer Electron System, Phys. Rev. Lett. **88**, 126804 (2002).

[24] J. A. Seamons, C. P. Morath, J. L. Reno, and M. P. Lilly, Coulomb Drag in the Exciton Regime in Electron-Hole Bilayers, Phys. Rev. Lett. **102**, 026804 (2009).

[25] D. Nandi, A. Finck, J. P. Eisenstein, L. N. Pfeiffer, and K. W. West, Exciton condensation and perfect Coulomb drag, Nature (London) **488**, 481 (2012).

[26] J. P. Eisenstein, G. S. Boebinger, L. N. Pfeiffer, K. W. West, and S. He, New Fractional Quantum Hall State in Double-Layer Two-Dimensional Electron Systems, Phys. Rev. Lett. **68**, 1383 (1992).

[27] Y. W. Suen, L. W. Engel, M. B. Santos, M. Shayegan, and D. C. Tsui, Observation of a $\nu = 1/2$ Fractional Quantum Hall State in a Double-Layer Electron System, Phys. Rev. Lett. **68**, 1379 (1992).

[28] D. Laroche, G. Gervais, M. Lilly, and J. Reno, 1D-1D Coulomb drag signature of a Luttinger liquid, Science **343**, 631 (2014).

[29] P. Debray, V. Zverev, O. Raichev, R. Klesse, P. Vasilopoulos, and R. Newrock, Experimental studies of Coulomb drag between ballistic quantum wires, J. Phys.: Condens. Matter **13**, 3389 (2001).

[30] M. Yamamoto, M. Stopa, Y. Tokura, Y. Hirayama, and S. Tarucha, Negative Coulomb drag in a one-dimensional wire, Science **313**, 204 (2006).

[31] K. Flensberg, Coulomb Drag of Luttinger Liquids and Quantum Hall Edges, Phys. Rev. Lett. **81**, 184 (1998).

[32] J.-M. Duan and S. Yip, Supercurrent Drag via the Coulomb Interaction, Phys. Rev. Lett. **70**, 3647 (1993).

[33] N. Giordano and J. D. Monnier, Cross-talk effects in superconductor–insulator–normal-metal trilayers, Phys. Rev. B **50**, 9363 (1994).

[34] X. Huang, G. Bazàn, and G. H. Bernstein, Observation of Supercurrent Drag between Normal Metal and Superconducting Films, Phys. Rev. Lett. **74**, 4051 (1995).

[35] E. Shimshoni, Role of vortices in the mutual coupling of superconducting and normal-metal films, Phys. Rev. B **51**, 9415 (1995).

[36] A. Kamenev and Y. Oreg, Coulomb drag in normal metals and superconductors: Diagrammatic approach, Phys. Rev. B **52**, 7516 (1995).

[37] A. M. Lobos and T. Giamarchi, Dissipative phase fluctuations in superconducting wires capacitively coupled to diffusive metals, Phys. Rev. B **82**, 104517 (2010).

[38] A. Levchenko and M. R. Norman, Proposed Giaever transformer to probe the pseudogap phase of cuprates, Phys. Rev. B **83**, 100506(R) (2011).

[39] R. Gorbachev, A. Geim, M. Katsnelson, K. Novoselov, T. Tudorovskiy, I. Grigorieva, A. H. MacDonald, S. Morozov, K. Watanabe, T. Taniguchi *et al.*, Strong Coulomb drag and broken symmetry in double-layer graphene, Nat. Phys. **8**, 896 (2012).

[40] M. Titov, R. V. Gorbachev, B. N. Narozhny, T. Tudorovskiy, M. Schütt, P. M. Ostrovsky, I. V. Gornyi, A. D. Mirlin, M. I. Katsnelson, K. S. Novoselov, A. K. Geim, and L. A. Ponomarenko, Giant Magnetodrag in Graphene at Charge Neutrality, Phys. Rev. Lett. **111**, 166601 (2013).

[41] X. Liu, K. Watanabe, T. Taniguchi, B. I. Halperin, and P. Kim, Quantum Hall drag of exciton condensate in graphene, Nat. Phys. **13**, 746 (2017).

[42] J. Li, T. Taniguchi, K. Watanabe, J. Hone, and C. Dean, Excitonic superfluid phase in double bilayer graphene, Nat. Phys. **13**, 751 (2017).

[43] Y. Cao, V. Fatemi, S. Fang, K. Watanabe, T. Taniguchi, E. Kaxiras, and P. Jarillo-Herrero, Unconventional superconductivity in magic-angle graphene superlattices, Nature (London) **556**, 43 (2018).

[44] Y. Cao, V. Fatemi, A. Demir, S. Fang, S. L. Tomarken, J. Y. Luo, J. D. Sanchez-Yamagishi, K. Watanabe, T. Taniguchi, E. Kaxiras *et al.*, Correlated insulator behaviour at half-filling in magic-angle graphene superlattices, Nature (London) **556**, 80 (2018).

[45] Y.-Y. Pai, A. Tylan-Tyler, P. Irvin, and J. Levy, Physics of $SrTiO_3$-based heterostructures and nanostructures: A review, Rep. Prog. Phys. **81**, 036503 (2018).

[46] A. Caviglia, S. Gariglio, N. Reyren, D. Jaccard, T. Schneider, M. Gabay, S. Thiel, G. Hammerl, J. Mannhart, and J.-M. Triscone, Electric field control of the $LaAlO_3/SrTiO_3$ interface ground state, Nature (London) **456**, 624 (2008).

[47] N. Reyren, S. Thiel, A. Caviglia, L. F. Kourkoutis, G. Hammerl, C. Richter, C. Schneider, T. Kopp, A.-S. Rüetschi, D. Jaccard *et al.*, Superconducting interfaces between insulating oxides, Science **317**, 1196 (2007).

[48] A. Brinkman, M. Huijben, M. Van Zalk, J. Huijben, U. Zeitler, J. Maan, W. G. van der Wiel, G. Rijnders, D. H. Blank, and H. Hilgenkamp, Magnetic effects at the interface between nonmagnetic oxides, Nat. Mater. **6**, 493 (2007).

[49] A. D. Caviglia, M. Gabay, S. Gariglio, N. Reyren, C. Cancellieri, and J.-M. Triscone, Tunable Rashba Spin-Orbit Interaction at Oxide Interfaces, Phys. Rev. Lett. **104**, 126803 (2010).

[50] S. Thiel, G. Hammerl, A. Schmehl, C. W. Schneider, and J. Mannhart, Tunable quasi-two-dimensional electron gases in oxide heterostructures, Science **313**, 1942 (2006).

[51] C. Cen, S. Thiel, G. Hammerl, C. W. Schneider, K. Andersen, C. Hellberg, J. Mannhart, and J. Levy, Nanoscale control of an interfacial metal–insulator transition at room temperature, Nat. Mater. **7**, 298 (2008).

[52] C. Cen, S. Thiel, J. Mannhart, and J. Levy, Oxide nanoelectronics on demand, Science **323**, 1026 (2009).

[53] F. Bi, D. F. Bogorin, C. Cen, C. W. Bark, J.-W. Park, C.-B. Eom, and J. Levy, "Water-cycle" mechanism for writing and erasing nanostructures at the $LaAlO_3/SrTiO_3$ interface, Appl. Phys. Lett. **97**, 173110 (2010).

[54] Y. Tang, J.-W. Lee, A. Tylan-Tyler, H. Lee, M. Tomczyk, M. Huang, C.-B. Eom, P. Irvin, and J. Levy, Frictional drag between superconducting $LaAlO_3/SrTiO_3$ nanowires, Semicond. Sci. Technol. **35**, 09LT01 (2020).

[55] G. Jnawali, M. Huang, J.-F. Hsu, H. Lee, J.-W. Lee, P. Irvin, C.-B. Eom, B. D'Urso, and J. Levy, Room-temperature quantum

transport signatures in graphene/$LaAlO_3$/$SrTiO_3$ heterostructures, Adv. Mater. **29**, 1603488 (2017).

[56] G. Jnawali, H. Lee, J.-W. Lee, M. Huang, J.-F. Hsu, F. Bi, R. Zhou, G. Cheng, B. D'Urso, P. Irvin *et al.*, Graphene-complex-oxide nanoscale device concepts, ACS Nano **12**, 6128 (2018).

[57] S. Dhingra, J.-F. Hsu, I. Vlassiouk, and B. D'Urso, Chemical vapor deposition of graphene on large-domain ultra-flat copper, Carbon **69**, 188 (2014).

[58] M. Huang, G. Jnawali, J.-F. Hsu, S. Dhingra, H. Lee, S. Ryu, F. Bi, F. Ghahari, J. Ravichandran, L. Chen, P. Kim, C.-B. Eom, B. D'Urso, P. Irvin, and J. Levy, Electric field effects in graphene/$LaAlO_3$/$SrTiO_3$ heterostructures and nanostructures, APL Mater. **3**, 062502 (2015).

[59] J. Li, Q. Guo, L. Chen, S. Hao, Y. Hu, J.-F. Hsu, H. Lee, J.-W. Lee, C.-B. Eom, B. D'Urso *et al.*, Reconfigurable edge-state engineering in graphene using $LaAlO_3$/$SrTiO_3$ nanostructures, Appl. Phys. Lett. **114**, 123103 (2019).

[60] S. Kim and E. Tutuc, Coulomb drag and magnetotransport in graphene double layers, Solid State Commun. **152**, 1283 (2012).

[61] B. L. Altshuler, P. A. Lee, and W. R. Webb, *Mesoscopic Phenomena in Solids* (Elsevier, Amsterdam, 2012).

[62] A. Price, A. Savchenko, B. N. Narozhny, G. Allison, and D. Ritchie, Giant fluctuations of Coulomb drag in a bilayer system, Science **316**, 99 (2007).

[63] V. K. Guduru, Surprising magnetotransport in oxide heterostructures, Ph.D. thesis, Radboud University Nijmegen, 2014.

[64] G. Cheng, M. Tomczyk, A. B. Tacla, H. Lee, S. Lu, J. P. Veazey, M. Huang, P. Irvin, S. Ryu, C.-B. Eom, A. Daley, D. Pekker, and J. Levy, Tunable Electron-Electron Interactions in $LaAlO_3$/$SrTiO_3$ Nanostructures, Phys. Rev. X **6**, 041042 (2016).

[65] Z. Jiang, Y. Zhang, Y.-W. Tan, H. Stormer, and P. Kim, Quantum Hall effect in graphene, Solid State Commun. **143**, 14 (2007).

[66] J. Moser, A. Barreiro, and A. Bachtold, Current-induced cleaning of graphene, Appl. Phys. Lett. **91**, 163513 (2007).

[67] C. W. Groth, M. Wimmer, A. R. Akhmerov, and X. Waintal, Kwant: A software package for quantum transport, New J. Phys. **16**, 063065 (2014).

[68] R. Tao, L. Li, H.-Y. Xie, X. Fan, L. Guo, L. Zhu, Y. Yan, Z. Zhang, and C. Zeng, Josephson-Coulomb drag effect between graphene and $LaAlO_3$/$SrTiO_3$ interfacial superconductor, arXiv:2003.12826.

[69] H. C. Tso, P. Vasilopoulos, and F. M. Peeters, Direct Coulomb and Phonon-Mediated Coupling between Spatially Separated Electron Gases, Phys. Rev. Lett. **68**, 2516 (1992).

[70] H. C. Tso, P. Vasilopoulos, and P. Peeters, Coupled electron-hole transport: Generalized random-phase approximation and density functional theory, Surf. Sci. **305**, 400 (1994).